INTERNATIONAL JOURNAL FOR NUMERICAL AND ANALYTICAL METHODS IN GEOMECHANICS
Int. J. Numer. Anal. Meth. Geomech., 2003; **27**:1099–1122 (DOI: 10.1002/nag.316)

Fabric evolution of granular assembly under K_0 loading/unloading

Jyh-Chau Liou[†] and Yii-Wen Pan[*,‡,§]

Department of Civil Engineering, National Chiao-Tung University, 1001 Ta-Hsueh Road, Hsinchu 30050, Taiwan

SUMMARY

This study attempted to investigate the fabric evolution in K_0 loading/unloading. The work made use of a field simulator to control K_0 loading/unloading in large specimens prepared by air-pluviation. In each loading stage, wave velocities along various propagation directions were measured. On the basis of the theories of micro-mechanics and wave propagation, the microscopic parameters of the granular assembly were back calculated to investigate the fabric evolution of granular soil during K_0 loading/unloading.

In this study, the Geometric fabric was modelled by fabric tensors of ranks 2 and 4. The comparison of calibrated results using ranks 2 and 4 revealed the advantage of the usage of rank-4 fabric tensor in modelling fabric evolution in spite of its complexity.

By comparing relative magnitudes of vertical and horizontal components of geometric fabric, it was demonstrated that relative constraint in lateral directions increased during K_0-unloading in order to maintain a K_0 condition. It revealed that fabric evolution was responsible for a higher K_0 in unloading than K_0 in loading. Copyright © 2003 John Wiley & Sons, Ltd.

KEY WORDS: fabric evolution; K_0 condition; granular assembly; micromechanics; fabric tensor; wave propagation

1. INTRODUCTION

The packing or microscopic structures of a granular material determine its mechanical behaviour. The packing state of a granular assembly has been named 'structure' or 'fabric' in various references, and can be described by void ratio and contact normal distribution. Void ratio is a scalar state quantity; it can reflect the average contact number (coordination number). On the other hand, the contact normal distribution is a directional data. Although general fabric should include void ration and the contact normal distribution, the latter is the primary concern of the fabric of a granular material.

*Correspondence to: Yii-Wen Pan, Department of Civil Engineering, National Chiao-Tung University, 1001 Ta-Hsueh Road, Hsinchu 30050, Taiwan.
[†]PhD Student.
[‡]E-mail: ywpan@cc.nctu.edu.tw
[§]Professor.

Contract/grant sponsor: National Science Council of the Republic of China; contract/grant number: NSC90-2211-E-009-068

Received 5 February 2003
Revised 30 May 2003
Accepted 23 June 2003

Many researchers have adopted the micro-mechanics theory to investigate the mechanical behaviour of a granular assembly from a microscopic viewpoint [1–7]. Various factors can affect the mechanical behaviour of a granular assembly; these factors may include particle properties, fabric and stress state. For given particle properties, fabric and stress state of a granular assembly dominate its mechanical behaviour. Since both fabric and stress state are directional data, they also control the anisotropy in mechanical behaviour. Fabric and stress state, respectively, can be regarded as the internal index and the external index for determining the mechanical behaviour of a granular assembly.

Fabric evolution of a granular assembly subjected to loading can help understand the mechanism of its mechanical behaviour during loadings. The techniques for estimating fabric of a granular assembly can be categorized into direct and indirect methods in general [3, 8–14]. Pan and Dong [14] discussed the capability and limitation of these techniques. The direct methods can measure two-dimensional fabric, but might find it difficult to reconstruct three-dimensional fabric. Some indirect methods may be used to evaluate three-dimensional fabric by means of the incorporation of certain quantitative model. Among various indirect methods, it is possible to make use of wave-velocity measurement technique on the basis of micro-mechanics theory to estimate both the geometric fabric and the contact-force fabric of a granular material such as sand.

The elastic stiffness for a granular material is a function of its microscopic parameters and stress state. While the wave velocities for a granular material depend on its elastic stiffness, it is reasonable to infer that the wave velocity of a granular assembly is also a function of its stress state and microscopic parameters, including the fabric and the state parameters related to inter-particle contact state.

The present work made use of a servo-controlled axis-symmetric simulator [15] to carry out a series of K_0 loading tests for specimens with various relative densities. In this work, a specimen was subjected to stress paths in K_0 loading and unloading. During various loading/unloading stages, the wave velocities in various directions were measured by means of miniature geophones. On the basis of theories including wave propagation, micro-mechanics, and optimization, the microscopic parameters of the granular assembly were back calculated to investigate the fabric evolution of granular soil during K_0 loading/unloading. The following context includes the theoretical background, experimental set-up, results, discussions and conclusions.

2. THEORETICAL BACKGROUND

The presented approach estimated fabric parameters from measured anisotropic wave velocities and stress state; this approach involved an analytical procedure similar to the one proposed by Pan and Dong [14]. Figure 1 outlines the conceptual procedure.

This section will briefly discuss the relevant theoretical background of the present study including fabric description and an outline of micro-mechanics of granular assembly, anisotropic wave propagation and optimization.

2.1. Fabric description

The distribution of directional data, such as the contact normal of a granular assembly, can be described in tensor forms [16], a Fourier series [17], or a spherical harmonics expansion [18].

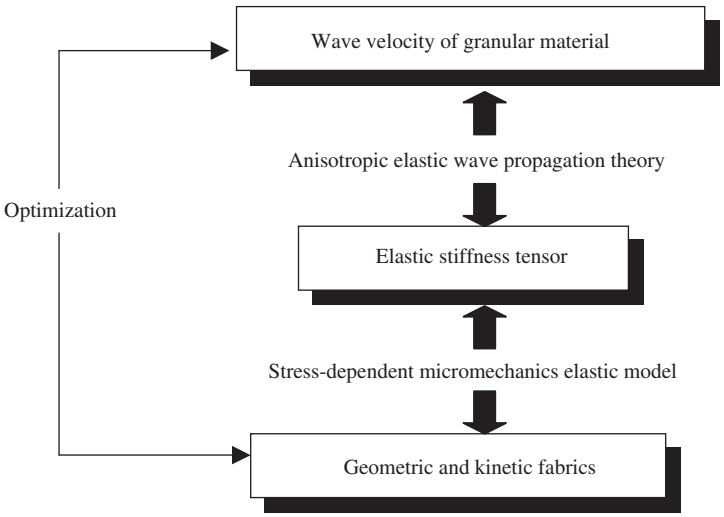

Figure 1. Analytical procedure for determining geometric and kinetic fabrics of a granular material from measured wave velocity [14].

This study adopted fabric tensors of the third kind to describe the distribution density of contact normal as the following expression:

$$E(\mathbf{n}) = C(D + D_{ij}n_in_j + D_{ijkl}n_in_jn_kn_l + \cdots) \tag{1}$$

Equation (1) is a spherical harmonics expansion. The notation '$\mathbf{n}$' denotes a unit directional vector. Since $E(\mathbf{n})$ represents a density function of directional data, $\int E(\mathbf{n}) \cdot \mathrm{d}\mathbf{n} = 1$ must be satisfied, thus C is equal to $1/2\pi$ and $1/4\pi$ for the case of two and three dimensions, respectively. The coefficient tensor $D_{i_1 \cdots i_n}$ is called the 'fabric tensor of the third kind' of rank n. The coefficient tensor D, i.e. the fabric tensor of the third kind of rank 0, must be 1. The coefficient tensors in the three-dimensional case are as follows:

$$D = 1 \tag{2}$$

$$D_{ij} = \tfrac{15}{2}\left[N_{ij} - \tfrac{1}{3}\delta_{ij}\right] \tag{3}$$

$$D_{ijkl} = \tfrac{315}{8}\left[N_{ijkl} - \tfrac{6}{7}\delta_{(ij}N_{kl)} + \tfrac{3}{35}\delta_{(ij}\delta_{kl)}\right]$$

$$\vdots \tag{4}$$

in which δ_{ij} is Kronecker delta tensor, $N_{i_1,i_2 \cdots i_n}$ is called the 'fabric tensor of the first kind' of rank n which represents the average of their tensor product, i.e.

$$N_{i_1 i_2 \cdots i_n} = \int n_{i_1} \cdots n_{i_n} E(\mathbf{n}) \cdot \mathrm{d}\mathbf{n}$$

A granular assembly prepared by pluviation may behave as transversely isotropic material. Figure 2 shows the co-ordinate system of a transversely isotropic material: axis 3 is the direction of pluviation and plane 1–2 is the plane of transverse isotropy. The coefficient tensors D_{ij} of a

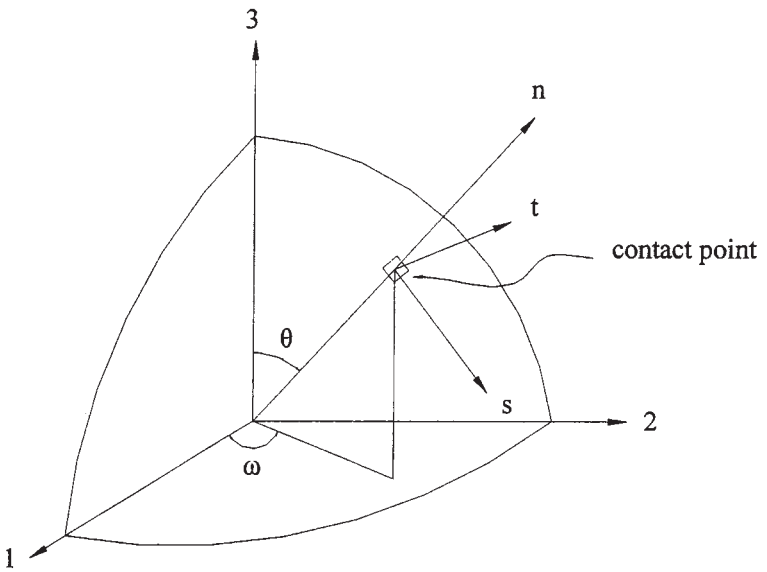

Figure 2. Spherical co-ordinate system.

transversely isotropic material must satisfy $D_{11} = D_{22}$, and $D_{12} = D_{21} = D_{13} = D_{31} = D_{23} = D_{32} = 0$ due to axis-symmetry. The condition $\int E(\mathbf{n}) \cdot \mathrm{d}\mathbf{n} = 1$ yields.

$$D_{11} = D_{22} = -D_{33}/2 \tag{5}$$

If the distribution of directional data is approximated by a fabric tensor of rank 2, Equation (1) is reduced to $E(\mathbf{n}) = (1 + D_{ij}n_i n_j)/4\pi$. Then, the independent unknown coefficient is solely D_{33}. A positive D_{33} implies that directional data is distributed more densely along the axis-3 direction than other directions, and vice versa. For a complete isotropic condition, all coefficient tensors of rank 2 are zero; thus Equation (1) is reduced to $E(\mathbf{n}) = 1/4\pi$.

For fabric tensor of rank 4, the coefficient tensors D_{ijkl} must satisfy $D_{1111} = D_{2222} = 3D_{1122}$ and $D_{1133} = D_{2233}$ due to transverse isotropy. Since Equation (3) must be satisfied, we can obtain three equations, i.e. $D_{1111} + D_{1122} + D_{1133} = 0$, $D_{2222} + D_{1122} + D_{2233} = 0$ and $D_{3333} + D_{1133} + D_{2233} = 0$. As a result,

$$D_{1111} = D_{2222} = 3D_{1122} = 3D_{3333}/8 \tag{6}$$

$$D_{1133} = D_{2233} = -D_{3333}/2 \tag{7}$$

If the distribution of directional data is approximated by a fabric tensor of rank 4, Equation (1) is reduced to $E(\mathbf{n}) = (1 + D_{ij}n_i n_j + D_{ijkl}n_i n_j n_k n_l)/4\pi$. The two independent unknown coefficient tensors are D_{33} and D_{3333}. The other components of fabric tensors are $D_{11} = D_{22} = -D_{33}/2$, $D_{1111} = D_{2222} = 3D_{1122} = 3D_{3333}/8$, $D_{1133} = D_{2233} = -D_{3333}/2$ and the rest of the coefficients are all zero. The fabric tensor of rank 4 will reduce to rank 2 if the coefficient tensor D_{3333} is equal to 0.

In this work, fabric tensors of ranks 2 and 4 were adopted to represent the contact-normal distribution. The fabric tensor of a higher rank usually is able to describe the shape of directional data distribution more closely.

2.2. Micro-mechanics theory of granular materials

It is possible to obtain the elastic stiffness of a granular assembly from its states of fabric and stress on the basis of micro-mechanics. An outline appears subsequently.

2.2.1. Elastic stiffness of a granular assembly. Chang and Misra [18] derived the elastic stiffness C_{ijkl} of a granular assembly composed of equal-sized spherical particles. C_{ijkl} is a function of contact stiffness and contact normal distribution, and can be expressed as follows

$$C_{ijkl} = \frac{1}{V}\sum_{c}^{M} \ell_i^c k_{jl}^c \ell_k^c = \frac{M}{V}\int_{\Omega} 4r^2 n_i k_{jl}^c n_k E(\mathbf{n}) \cdot \mathrm{d}\Omega \tag{8}$$

in which V is a representative volume, M is the contact number in V, $\ell_i^c = \ell \cdot n_i^{\tilde{l}} = 2 \cdot r \cdot n_i^c$ is the branch-vector connecting two adjacent particles' centroids in the cth contact point, r is the radius of the spherical particles, ℓ is the branch-vector-length and $n_i^{\tilde{l}}$ is the unit branch-vector identical with the contact normal n_i^c for an idealized granular assembly. The term $k_{jl}^c = k_n^c n_j^c n_l^c + k_s^c s_j^c s_l^c + k_t^c t_j^c t_l^c$ is the local contact stiffness. The components k_n^c, k_s^c and k_t^c, respectively, are the contact stiffness along the directions of **n**, **s** and **t**, which are the three base vectors of the local co-ordinate system shown in Figure 2. The term $E(\mathbf{n})$ stands for the density function of the contact normal in the **n** direction. The terms $E(\mathbf{n})$ can be expressed as $E(\omega, \theta)$; $\mathrm{d}\Omega = \sin\theta\, \mathrm{d}\omega\, \mathrm{d}\theta$ in a spherical co-ordinate system, where ω and θ are defined in Figure 2, with the ranges $0 \leqslant \omega \leqslant 2\pi$ and $0 \leqslant \theta \leqslant \pi$. Pan and Dong [14] further derived the derivation of C_{ijkl} of a granular assembly composed of graded spherical particles.

2.2.2. Contact stiffness. Using the Hertz–Mindlin theory, the normal contact stiffness $k_n(\mathbf{n})$ and shear contact stiffness $k_r(\mathbf{n})$ can be expressed as Equations (9) and (10), respectively.

$$k_n(\mathbf{n}) = C_1 (f_n(\mathbf{n}))^{1-2\alpha} \tag{9}$$

$$k_r(\mathbf{n}) = C_2 \left(1 - \frac{f_r(\mathbf{n})}{f_n(\mathbf{n}) \tan\phi_\mu}\right)^{\beta} \cdot k_n(\mathbf{n}) \tag{10}$$

in which $f_n(\mathbf{n})$ and $f_r(\mathbf{n})$ are the normal and shear contact forces, respectively; ϕ_μ is the inter-particle frictional angle; and C_1 and C_2 are constants relating to particle property.

2.2.3. Contact force. The contact forces in Equations (9) and (10) can be estimated using a localized procedure of stresses and can be expressed as follows:

$$f_j^c = \sigma_{ij} A_{ik} n_k^c \tag{11}$$

in which f_j^c is the contact force, σ_{ij} is the stress tensor and A_{ik} is a tensor relating to geometric fabric of the granular assembly.

2.3. Theory of elastic wave propagation for anisotropic material

If axis-3 is the symmetrical axis of a transversely isotropic granular assembly, five elastic constants, E_{11}, E_{33}, E_{12}, E_{23} and E_{66}, are independent. All other elastic constants can be related to these five constants according to the following relations: $E_{22} = E_{11}$, $E_{13} = E_{23}$, $E_{55} = E_{66}$, $E_{44} = (E_{11} - E_{12})/2$ and the rest of elastic constants are zero. The elastic wave-velocity of a transversely isotropic material is dependent of the elastic constant and the angle θ between

the rotation-symmetry axis and the wave-propagation direction. The primary wave velocity $V_{p-\theta}$ and shear-wave velocities, $V_{\mathrm{sh}-\theta}$ and $V_{\mathrm{sv}-\theta}$, of elastic body wave can be expressed as follows [14]

$$V_{\mathrm{sh}-\theta} = \sqrt{(E_{66}\cos^2\theta + E_{44}\sin^2\theta)/\rho_d} \tag{12}$$

$$V_{p-\theta} = \sqrt{(-b + \sqrt{b^2 - 4c})/2\rho_d} \tag{13}$$

$$V_{\mathrm{sv}-\theta} = \sqrt{(-b - \sqrt{b^2 - 4c})/2\rho_d} \tag{14}$$

in which $b = -(E_{11}\sin^2\theta + E_{33}\cos^2\theta + E_{66})$, $c = (E_{11}\sin^2\theta + E_{66}\cos^2\theta)(E_{66}\sin^2\theta + E_{33}\cos^2\theta) - (E_{12} + E_{66})^2\cos^2\theta\sin^2\theta$; V_p, $V_{\mathrm{sh}-\theta}$, $V_{\mathrm{sv}-\theta}$ and θ are defined in Figure 3. In the remaining section, granular materials are assumed transversely isotropic.

2.4. Optimization method

Optimization aims to search for the optimized value of a non-linear object function $\Phi\{x\}$. In this study, $\Phi\{x\}$ is defined as a non-linear 'error square' function, which is the square sum of the differences between 'n' (model) calculated data, $U_i(\{x\})$, $(i = 1, n)$ and 'n' measured data of wave-velocity, $V_i, (i = 1, n)$ as follows.

$$\Phi\{x\} = \sum_{i=1}^{n} [U_i(\{x\}) - V_i]^2 \tag{15}$$

in which $\{x\}$ represents a vector containing the undetermined parameters; in this work, $\{x\}$ contains α, β and D_{33} for fabric tensors of rank 2, and contains α, β, D_{33}, and D_{3333} for fabric

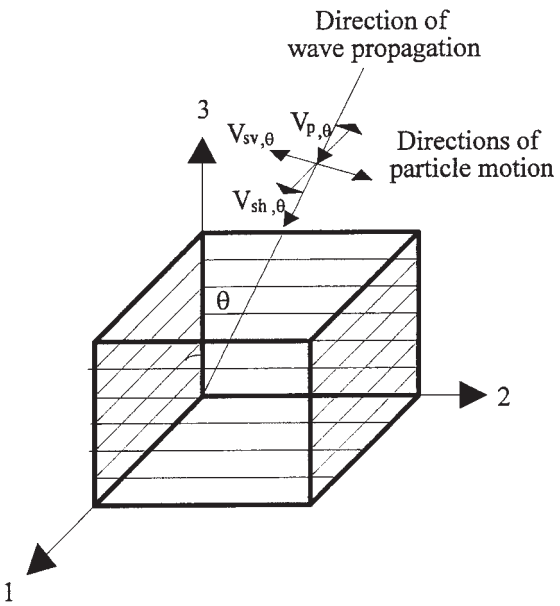

Figure 3. Directions of primary and shear wave propagation and polarization through a transversely isotropic material [14].

tensors of rank 4. The involved non-linear optimization aims to search for a set of $\{x\}$ corresponding to a series of $U_i(\{x\})$, $(i = 1, n)$ such that the error square function can be minimized.

This study made use of a two-step optimization procedure combining the genetic algorithm [19] with non-linear optimization by the Levenberg-Marquardt method [20] to search for the most suitable microscopic parameters from a set of measured wave velocities. The optimization procedure began with the genetic algorithm in order to obtain a number of solutions as candidates. Subsequently, these candidates were planted as the initial guess of solution in the non-linear optimization method in order to refine the solution. This combined use of optimization worked well.

3. EXPERIMENTAL SET-UP AND PROCEDURE

The sample used in the tests was Ottawa Sand (C-109) with the index properties listed in Table I. A series of laboratory tests made use of a set-up of axis-symmetric field simulator [15] to house the test specimen and control the K_0 loading condition. The simulator is a close-loop system that is capable of controlling various lateral boundary conditions. Figure 4 shows the layout of the field simulator. The sand specimen, 790 mm in diameter and up to 910 mm high, is housed in a stack of 11 rings made of steel; each ring (80.5 mm high) is lined with an inflatable silicone rubber membrane on the inside to allow circumferential displacement (extensometer) measurement and stress control (by air pressure). Specimens were prepared by dry pluviation using a sand-rainer. The relative density of the specimen was controlled by the opening slot size of the sand-rainer's base. Specimens of three different relative densities, i.e. $D_r = 95\%$ ($e = 0.513$), $D_r = 62.3\%$ ($e = 0.598$) and $D_r = 46.5\%$ ($e = 0.639$), were prepared and tested in this study.

The equipment for measuring wave velocities included a wave generator, an amplifier, and a series of geophones (served as both the wave activators and the receivers) and a spectrum analyser. Figure 5 shows the configuration of test equipment. The wave velocity was determined by dividing the distance between the wave activator and receiver by the travel time between them. Figure 6 shows the layout of geophones. In each specimen, twenty-two geophones were installed in five subsequent layers. The pluviation for preparing the specimen proceeded in six stages. As the specimen reached a specific elevation, the pluviation was halted and the geophones were installed. Their locations were engineered to measure wave velocity propagating along various directions.

Table I. Properties of Ottawa Sand (C-109).

Mineral	Quartz
Shape	Rounded
e_{max}	0.76
e_{min}	0.50
G_s	2.65
D_{60}(mm)	0.36
D_{10}(mm)	0.23
C_u	1.56

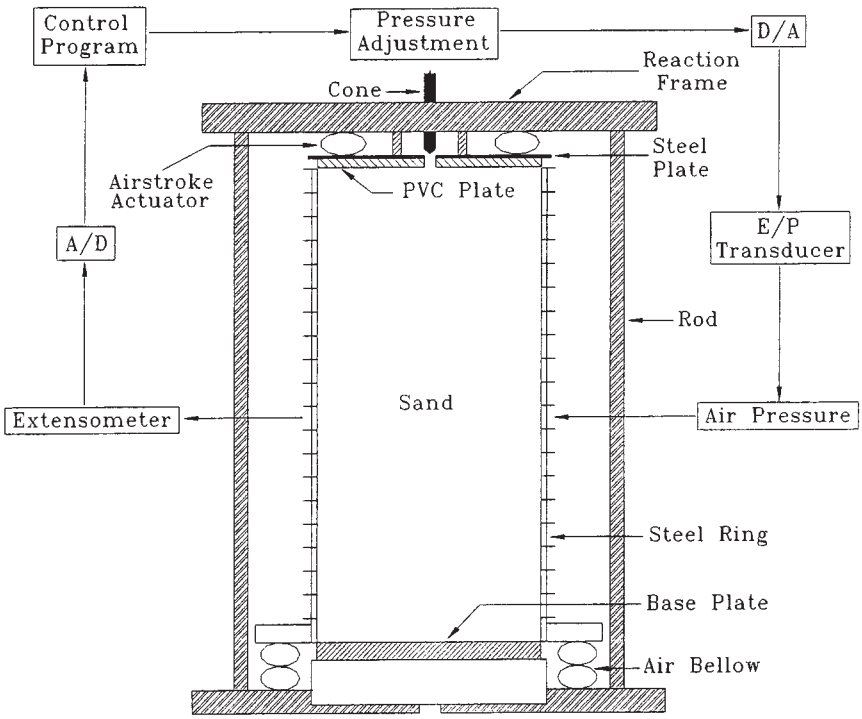

Figure 4. Layout of field simulator [15].

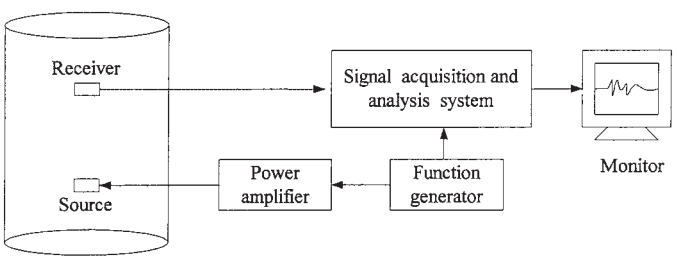

Figure 5. Layout of equipments.

During the whole course of a test (including the air-pluviated preparation of specimen and the application of loading), the lateral boundary of specimen was maintained at a near K_0 condition. The lateral stress in rings was adjusted to allow the circumferential deformation within ± 0.005 mm (corresponding to a strain within $\pm 2 \times 10^{-6}$). The threshold deformation was able to simulate K_0 condition and immune from the influence of signal noise.

The vertical loading was applied in a sequence of 0 kPa $\rightarrow$ 26.73 kPa $\rightarrow$ 51.7 kPa $\rightarrow$ 100.05 kPa $\rightarrow$ 51.7 kPa $\rightarrow$ 26.73 kPa $\rightarrow$ 0 kPa while the specimen was maintained in a K_0 condition. In addition to the applied loading, the specimen was subjected to an initial stress from its

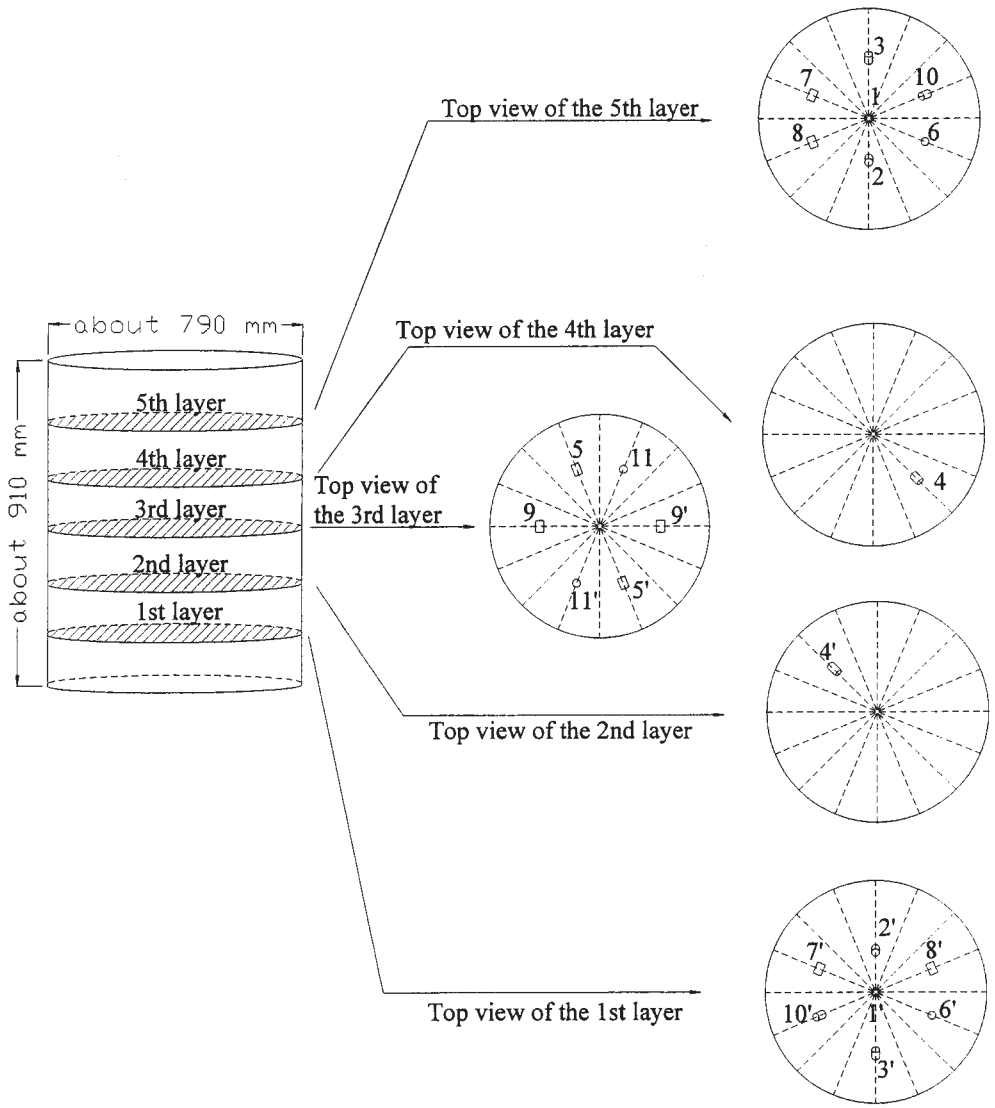

Figure 6. Layout of geophones in a specimen.

self-weight and the weight of top plate, which made a total of 10.49 kPa for $D_r = 46.5\%$, 10.67 kPa for $D_r = 62.3\%$ or 11.08 kPa for $D_r = 95\%$. For each loading stage, the P- and S-wave velocities between each pair of the source and receiver geophones were measured to obtain wave velocities along various directions of wave-propagation. The size of the field simulator inevitably limited the maximum number of installed geophones; a total of ten wave velocities were measured, including five P-wave velocities, three SH-wave velocities, and two SV-wave velocities along various wave-propagation directions.

4. RESULTS AND ANALYSIS

4.1. Sample characteristics

The sample used in this study is Ottawa sand composed of nearly pure quartz. The elastic constants of the particles were assumed as the elastic constants of crystal quartz with $E_s = 86.85$ GPa[¶] and $G_s = 31.14$ GPa (see footnote ¶), the corresponding Poisson's ratio, v_s, is 0.39. The frictional angle between quartz particles is 26° [21]. Oda [22] concluded that the average co-ordination number, N, of a granular assembly had a strong correlation with void ratio e, and was not affected by the grain-size distribution. Chang *et al*. [2] collected published data [22–24] and suggested N can be estimated from void ratio using the following equation:

$$e = 1.66 - 0.125N \tag{16}$$

This work adopted the empirical equatión of Chang *et al*. [2] to evaluate N.

4.2. Measured wave velocities

In each specimen, P- and S-wave velocities along various directions were measured by means of geophones embedded in the specimen. Figures 7–12 present the results of wave velocity measurements. Figures 7–9 show the wave-velocity distributions in loading stages, while Figures 10–12 show the distributions in unloading stages. In these figures, 'V_{p-m}' and 'V_{sh-m}', respectively, denote the measured P- and SH-wave velocities. The calculated wave-velocity distributions are also included in these figures for comparison and will be discussed in the latter context.

4.3. Measured stresses

A stack of eleven rings housed the tested specimen. To minimize the boundary effect, the results of stress measurements near the top and bottom were ignored. Only the results in the seven intermediate rings were picked up for the analysis of stresses. Columns 3, 4, and 5 in Table II compile the applied vertical stress σ_v, the average (measured) horizontal stress $(\sigma_h)_{ave}$, and the K_0 obtained for the specimens of various D_r. The comparison of the measured K_0 clearly demonstrated two trends: (1) a specimen with a higher D_r has a lower K_0 and their relation agrees well with the Jaky's formula, $K_0 = 1 - \sin\phi'$, by taking into account the relation between D_r and ϕ'; and (2) K_0 during unloading is significantly larger than K_0 during loading.

5. CALCULATED RESULTS AND DISCUSSION

In the present work, a specimen was maintained in a K_0 condition with controlled vertical stress. The unknown parameters were back calculated from the measured wave velocities and stress state. Since these unknown parameters describe the contact status of a granular assembly, they are termed 'microscopic parameters' hereafter. These microscopic parameters include D_{33} (for fabric tensor of rank 2) or D_{33}/D_{3333} (for fabric tensor of rank 4), the normal contact stiffness α and the shear contact stiffness β.

[¶] data from http://www.crystran.co.uk/qutzdata.htm.

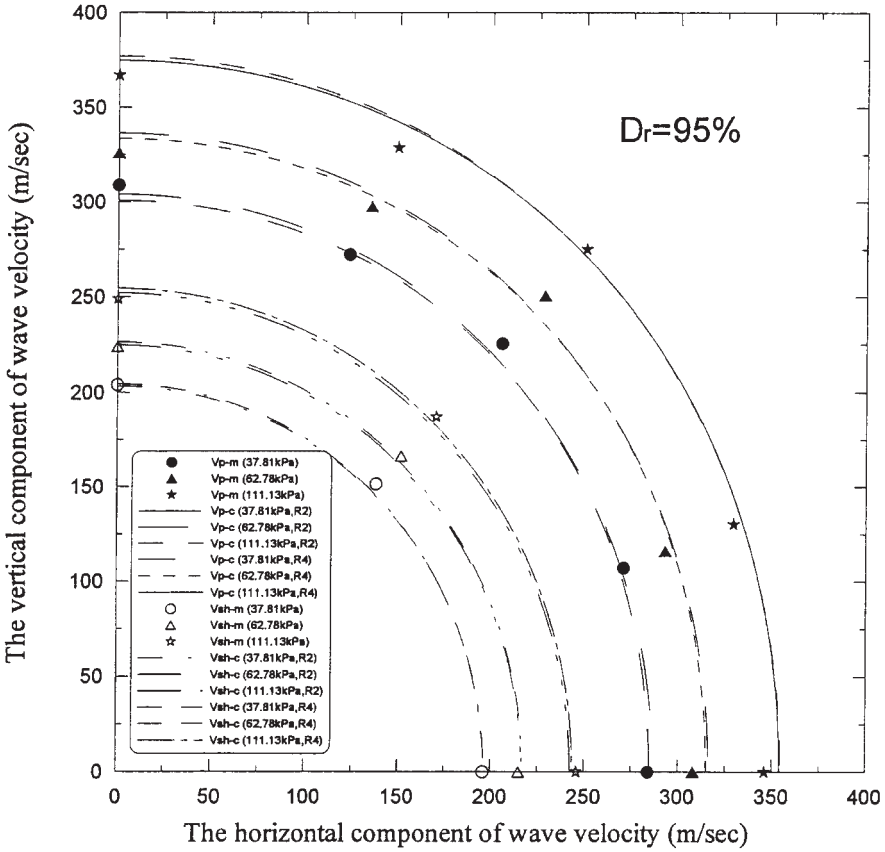

Figure 7. Comparison of the calculated and measured wave velocity distributions in various loading stages for $D_r = 95\%$.

The last four columns in Table II list the calibrated results for various cases. To examine the adequacy of the calibrated results, the wave velocities calculated with the calibrated parameters were compared with the measured wave velocities in Figures 7 through 12. For loading stages, the measured data set altogether were used to calibrate the average microscopic parameters. Figures 7, 8 and 9, respectively, compare the distributions of the calculated and measured wave velocities in loading stages for $D_r = 95\%$, $D_r = 62.3\%$ and $D_r = 46.5\%$; while Figures 10, 11 and 12, respectively, compare the distributions of the calculated and measured wave velocities in unloading stages for $D_r = 95\%$, $D_r = 62.3\%$ and $D_r = 46.5\%$. In these figures, 'V_{p-c}' and 'V_{sh-c}' denote the calculated P- and SH-wave, respectively; 'R2' denotes using fabric tensor of rank 2, 'R4' denotes using fabric tensor of rank 4.

Table III lists the average percentages of differences between the measured wave velocities and the wave velocities calculated with the calibrated parameters. The results' comparison indicated that the average percentages of differences using the fabric tensor of rank 4 were less than those using the fabric tensor of rank 2 in various loading stages for various relative densities. It clearly demonstrated that the distribution of wave velocities could be better

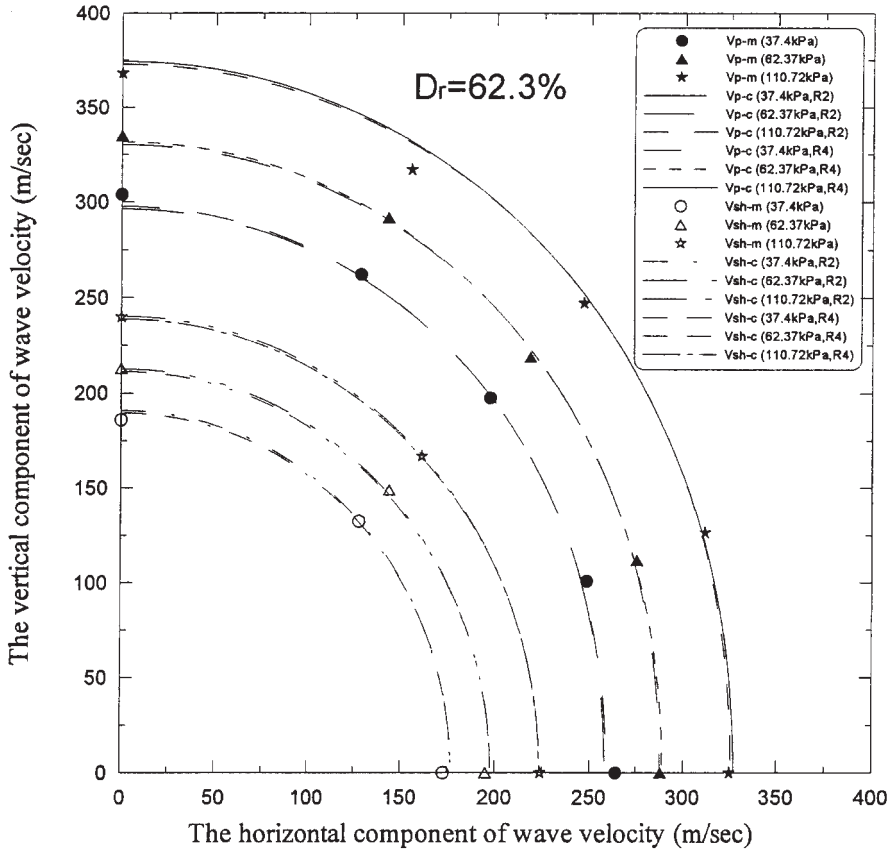

Figure 8. Comparison of the calculated and measured wave velocity distributions in various loading stages for $D_r = 62.3\%$.

modelled by using fabric tensor of rank 4 than rank 2 for describing the contact normal distribution.

Discussion on the calibrated results of microscopic parameters follows.

5.1. Normal contact stiffness parameter α

The normal contact stiffness can be expressed in the form of $k_n = C_1 \cdot f_n^{\gamma}$. According to the Hertz contact theory, γ equals to $\frac{1}{3}$; while γ should equal to $\frac{1}{2}$ based on the assumption of cone-to-plane contact [25]. Considering the contact mechanism of sand particles may be inelastic, non-linear, roughly contacted, and non-circular, Chang *et al.* [26] pointed out that the γ and C_1, respectively, for sand particles may be somewhat higher and lower, respectively, than what Hertz-Mindlin theory predicts [27]. Experimental data [28] supports that γ actually lies between $\frac{1}{3}$ and $\frac{1}{2}$. This study expressed the normal contact stiffness in the form of $k_n = C_1 f_n^{1-2\alpha}$, the parameter α should be within $\frac{1}{4}$ and $\frac{1}{3}$. Hence, for the calibration of α, the upper and lower bounds were set to $\frac{1}{3}$ and $\frac{1}{4}$ respectively. All calibrated α were between the upper and the lower limits.

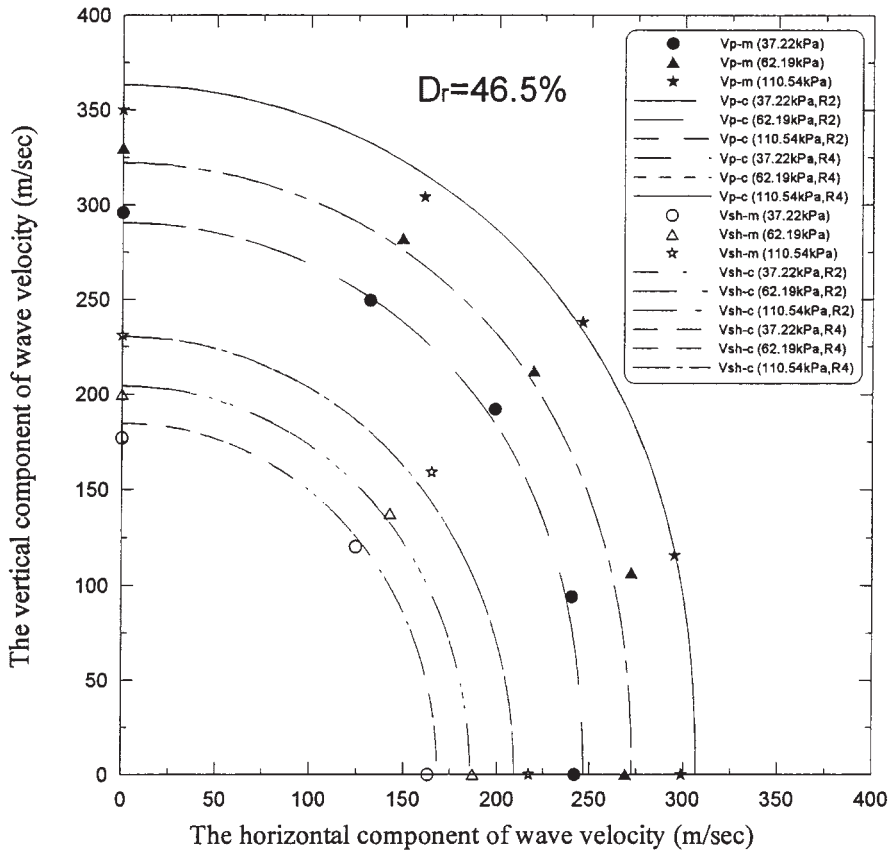

Figure 9. Comparison of the calculated and measured wave velocity distributions in various unloading stages for $D_r = 46.5\%$.

5.2. *Shear contact stiffness parameter* β

Mindlin and Deresiewicz [29] studied the shear contact compliance between two elastically contacted spheres under varying oblique forces. For a particulate assembly, however, every particle may contact with several other particles. It seems unlikely that all shear contact stiffness of particles can satisfy the shear contact relations derived by Mindlin and Deresiewicz [29]. Furthermore, it is difficult to employ the incremental form of shear contact relations practically. For these concerns, the present work expressed the shear contact stiffness in the following form.

$$k_r = C_2\left(1 - \frac{f_r}{f_n \tan \phi_\mu}\right)^{\beta} k_n \quad \text{as } f_r < f_n \tan \phi_\mu \tag{17}$$

$$k_r = 0 \quad \text{for } f_r \geqslant f_n \tan \phi_\mu \tag{18}$$

The shear contact stiffness parameter β should be non-negative; the condition $\beta = 0$ implied there was no local slippage that took place at the contact-point and the shear contact stiffness

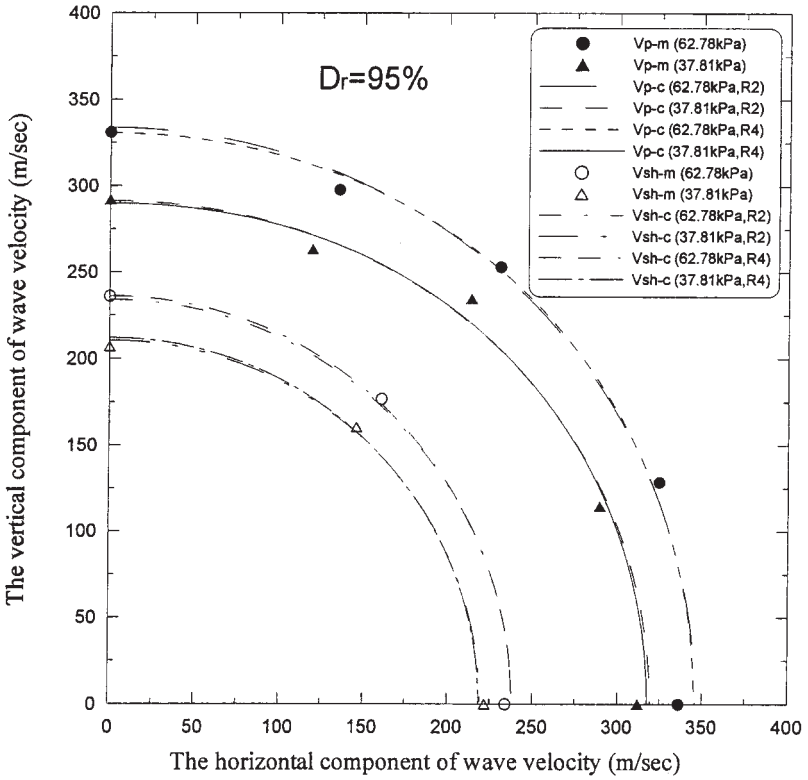

Figure 10. Comparison of the calculated and measured wave velocity distributions in various unloading stages for $D_r = 95\%$.

did not depend on the shear contact-force. Hence, the lower bound of β was set to 0. The calibrated β of a specimen with a higher D_r appears to be smaller. This is reasonable because a higher D_r (corresponding to a smaller void ratio) implies to a larger co-ordination number (according to Equation (16)), and will result in a stronger constraint to inter-particle slippage or rotation.

5.3. *Fabric parameter* D_{33}(*rank* 2) *or* D_{33}/D_{3333}(*rank* 4)

The fabric parameter D_{33} (rank 2) or D_{33}/D_{3333} (rank 4) determines the contact normal distribution in a granular assembly. Figures 13–15 show the calculated contact normal distributions after calibration. In these figures, 'L' denotes loading stage and 'U' denotes unloading stage. Discussions follow:

5.3.1. Fabric parameter of rank 2(D_{33}). In K_0 loading stages, D_{33} of very dense Ottawa sand ($D_r = 95\%$) was close to 0. It indicated that the contact normal distribution of the granular assembly at a very dense state tends to be rather isotropic or directionally uniform as shown in Figure 13(a). During K_0-unloading, however, D_{33} were negative; it indicated that the horizontal contact normal were more than the vertical contact normal, as shown in

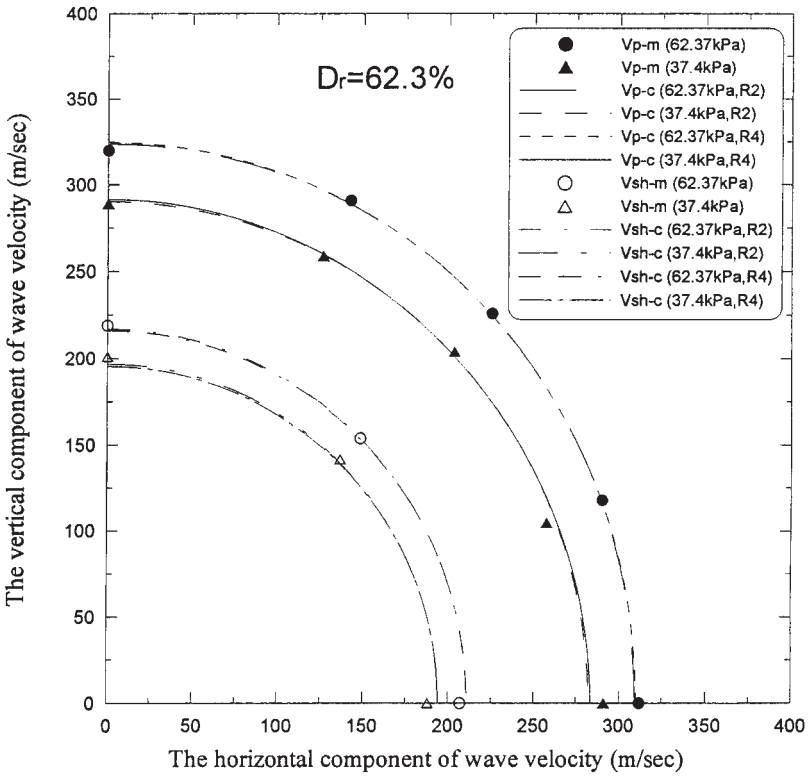

Figure 11. Comparison of the calculated and measured wave velocity distributions in various unloading stages for $D_r = 62.3\%$.

Figure 13(b) and 13(c). On the other hand, D_{33} in K_0-loading for medium dense or loose Ottawa sand ($D_r = 62.3\%$ and $D_r = 46.5\%$) were both positive. It implied that the number of contact points was significantly more abundant along the vertical direction than along the lateral direction as shown in Figures 14(a) and 15(a); it can also be noted that the Ottawa sand of lower D_r displayed a larger D_{33}. While in various unloading stages, in spite the shapes of their contact normal distributions were similar, D_{33} were smaller than the D_{33} in loading stages as shown in Figures 14(b)–(c) and 15(b)–(c). For example, D_{33} of $D_r = 62.3\%$ after K_0-unloading was reduced to near 0. A more pronounced difference in the contact density along various directions in a granular assembly would result in more anisotropic mechanical properties.

5.3.2. Fabric parameters of rank 4 (D_{33} *and* D_{3333}). The fabric coefficient D_{3333} may play a role of distorting the shape of density distribution in oblique directions, say $\theta = 45^\circ$. For negative D_{3333}, the shape of density distribution bulges outward in $\theta = 45^\circ$ direction, hence it resulted in an increase of the density in $\theta = 45^\circ$ direction and a decrease in both the vertical and horizontal directions; vice versa is true for a positive D_{3333}.

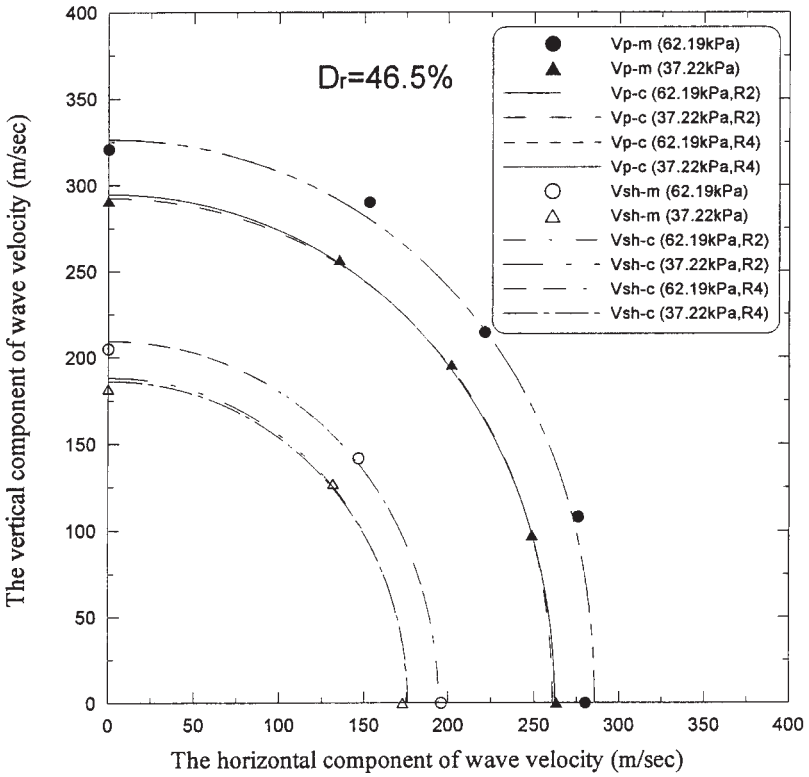

Figure 12. Comparison of the calculated and measured wave velocity distributions in various unloading stages for $D_r = 46.5\%$.

For $D_r = 95\%$ in K_0 loadings, contact normal distribution has its highest density in an oblique direction near $\theta = 45^\circ$, as shown in Figure 13(d). In this case, the resultant horizontal component is pretty close to the resultant vertical component. For K_0 unloading stages, the shape of density distribution remains similar to that in K_0 loading stages. However, the density in vertical direction decreases while the density in horizontal direction increases, as shown in Figure 13(e) and 13(f). The resultant horizontal component becomes larger than the resultant vertical component; this trend agrees with the case using rank 2.

For $D_r = 62.3\%$ in K_0 loadings, contact normal distribution has its lowest and highest densities in oblique (near $\theta = 45^\circ$) and vertical ($\theta = 0^\circ$) directions, respectively, as shown in Figure 14(d). For K_0 unloading, the density along oblique direction remains the lowest among all directions; also, the densities in vertical and horizontal directions get closer, as shown in Figure 14(e) and 14(f).

For $D_r = 46.5\%$ in K_0 loading, contact normal distribution has its highest and lowest densities in the vertical and horizontal directions, respectively, as shown in Figure 15(d). Since D_{3333} is close to 0, this contact normal distribution appears very similar to that using rank 2. In unloading, D_{3333} increases with decreasing σ_v; as a result, the density in oblique direction decreases with decreasing σ_v, as shown in Figure 15(e) and 15(f).

Table II. Experiment and calibrated results.

		σ_v (kPa)	$(\sigma_h)_{ave}$ (kPa)	K_0	Rank	Calibrated parameters			
						α	β	D_{33}	D_{3333}
$D_r = 95\%$	Loading stages	37.81	17.11	0.453	2	0.2956	0.029	−0.08	—
		62.78	26.97	0.430					
		111.13	46.49	0.418	4	0.2949	0	−0.01	−0.78
	Unloading stages	62.78	39.39	0.627	2	0.2958	0.014	−0.29	—
					4	0.2958	0.005	−0.25	−0.75
		37.81	28.80	0.762	2	0.2951	0.033	−0.42	—
					4	0.2948	0	−0.37	−0.62
$D_r = 62.3\%$	Loading stages	37.4	16.56	0.443	2	0.2918	0.062	0.23	—
		62.37	28.04	0.450					
		110.72	51.06	0.461	4	0.2922	0.106	0.19	0.48
	Unloading stages	62.37	41.71	0.669	2	0.2922	0.361	0.03	—
					4	0.2924	0.41	0.02	0.25
		37.4	30.26	0.809	2	0.2901	0.036	0.03	—
					4	0.2905	0.225	0.01	0.52
$D_r = 46.5\%$	Loading stages	37.22	19.46	0.523	2	0.2902	0.276	0.38	—
		62.19	30.70	0.494	4	0.2902	0.272	0.40	−0.01
		110.54	53.71	0.486					
	Unloading stages	62.19	38.26	0.615	2	0.2906	0.547	0.34	—
					4	0.2907	0.559	0.33	0.06
		37.22	25.43	0.683	2	0.2917	1.536	0.30	—
					4	0.2920	1.736	0.28	0.50

The above illustrations of the calibrated fabrics deserve more elaboration. Although less complicated, the distribution density for fabric of rank 2 is only capable of describing simpler shapes of fabric distribution such as round, elliptical or peanut-like shapes. Using fabric of rank 4 with D_{33} and D_{3333}, on the other hand, raises the flexibility for describing the shape of contact normal distribution.

Geometric fabrics calibrated using fabric of rank 4 for a very dense specimen ($D_r = 95\%$) showed that the densest distribution of geometric fabric is along an oblique direction, which was very different from those for looser specimens ($D_r = 62.3\%$ and $D_r = 46.5\%$). This may be attributed to the pluviation fabric and the applied shear stress level: the pluviation fabric of a very dense specimen was much more isotropic hence was likely to generate a bulged fabric near $\theta = 45^\circ$ direction when the specimen was subjected shear stress. A change in shear stress would increase or decrease the density of geometric fabric along the 45° direction, $E(\theta = 45^\circ)$, depending on the change in shear stress; for instance, $E(\theta = 45^\circ)$ for a specimen subjected to a larger shear stress, it should be larger than that for the same specimen subjected to a smaller shear stress. The influence of shear stress on geometric fabric can be examined by the relation between τ_{max}/σ_m (the maximum shear stress divided by the mean principal stress)

Table III. Average percentage of differences between the measured and the calculated wave velocities.

					Calibrated parameters				$\sqrt{\frac{\sum_{i=1}^{n}\left(\frac{V_m-V_c}{V_c}\right)^2}{n}}$
		σ_v (kPa)	K_0	Rank	α	β	D_{33}	D_{3333}	(%)
$D_r = 95\%$	Loading stages	37.81–111.13	0.418–0.453	2	0.2956	0.029	−0.08	—	1.786
				4	0.2949	0	−0.01	−0.78	1.699
	Unloading stages	62.78	0.627	2	0.2958	0.014	−0.29	—	1.974
				4	0.2958	0.005	−0.25	−0.75	1.644
		37.81	0.762	2	0.2951	0.033	−0.42	—	2.024
				4	0.2948	0	−0.37	−0.62	1.918
$D_r = 62.3\%$	Loading stages	37.4–110.72	0.443–0.461	2	0.2918	0.062	0.23	—	1.432
				4	0.2922	0.106	0.19	0.48	1.380
	Unloading stages	62.37	0.669	2	0.2922	0.361	0.03	—	1.123
				4	0.2924	0.41	0.02	0.25	1.098
		37.4	0.809	2	0.2901	0.036	0.03	—	2.089
				4	0.2905	0.225	0.01	0.52	2.047
$D_r = 46.5\%$	Loading stages	37.22–110.54	0.486–0.523	2	0.2902	0.276	0.38	—	2.180
				4	0.2902	0.272	0.40	−0.01	2.179
	Unloading stages	62.19	0.615	2	0.2906	0.547	0.34	—	1.462
				4	0.2907	0.559	0.33	0.06	1.461
		37.22	0.683	2	0.2917	1.536	0.30	—	1.395
				4	0.2920	1.736	0.28	0.50	1.230

and $E(\theta = 45^\circ)$. $E(\theta = 45^\circ)$ of a fully isotropic geometric fabric which is equal to $1/4\pi$. It can be noted that the normalized shear stress $(\sigma_v - \sigma_h)/(\sigma_v + \sigma_h)$ in the first unloading stage was larger than that in the second unloading stage, while $E(\theta = 45^\circ)$ of rank 4 at the first unloading stage was larger than that at the second unloading, as shown in Table IV. This trend cannot be predicted by fabric tensor of rank 2 because of its limitation. It reveals the superiority of the fabric tensor of rank 4 over rank 2 in modelling fabric evolution.

The role of geometric fabric on the stress state of K_0 loading/unloading was further explored. For this purpose, the total vertical component F_V and the total horizontal component F_H of geometric fabric were introduced. F_V was the resultant of the vertical component of geometric fabric in the upper half space projected onto the vertical axis (axis-3) $(= \int_0^{\pi/2} \int_0^{2\pi} \cos\theta\, E(\omega, \theta) \sin\theta\, d\omega\, d\theta)$ and F_H was the resultant of horizontal component of geometric fabric in the right (or left) half space projected on axis-1 or axis-2 (using a similar integral as the above but with an inter-changed integral domain). These integrations yielded the following results.

$$F_V = \frac{1}{4}\left(1 + \frac{D_{33}}{4} - \frac{D_{3333}}{24}\right) \tag{19}$$

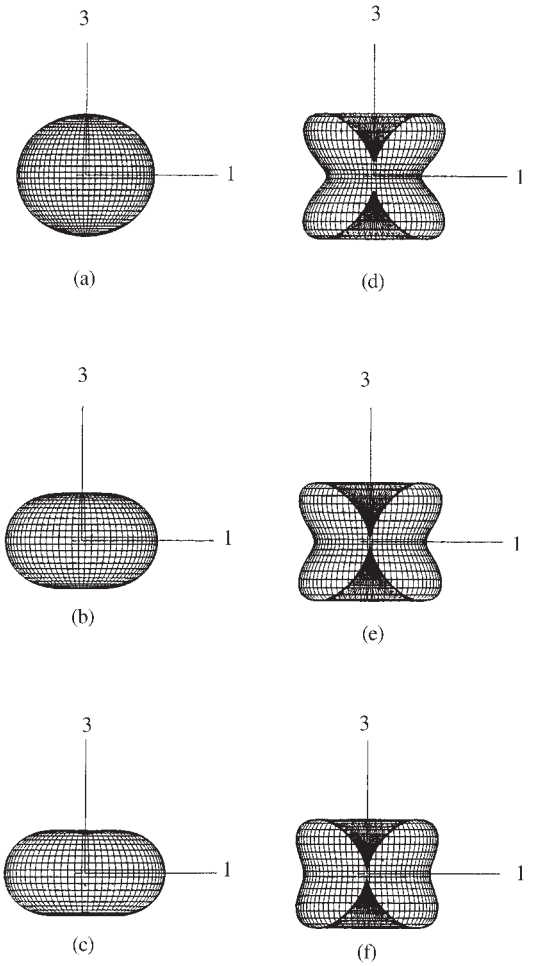

Figure 13. Evolutions of fabric of rank 2 ((a)–(c)) and rank 4 ((d)–(f)) in various loadings for $D_r = 95\%$: (a) $\sigma_v = 37.81$–111.13 kPa(L); (b) $\sigma_v = 62.78$ kPa(U); (c) $\sigma_v = 37.81$ kPa(U); (d) $\sigma_v = 37.81$–111.13 kPa(L); (e) $\sigma_v = 62.78$ kPa(U); and (f) $\sigma_v = 37.81$ kPa(U).

$$F_H = \frac{1}{4}\left(1 - \frac{D_{33}}{8} - \frac{D_{3333}}{64}\right) \tag{20}$$

For a fully isotropic geometric fabric, both F_H and F_V are equal to $\frac{1}{4}$, so the ratio F_H/F_V is equal to 1. Table V lists K_0, F_H, F_V and F_H/F_V for various cases. The ratio F_H/F_V in unloading appears significantly larger than in loading. Table V also shows that F_H/F_V increases with increasing K_0. The increasing ratio of F_H/F_V during unloading implies an increase of relative constraint in lateral directions in order to maintain a state of K_0 condition. This may be responsible for the fact that K_0 in unloading stages was always larger than K_0 in loading stage.

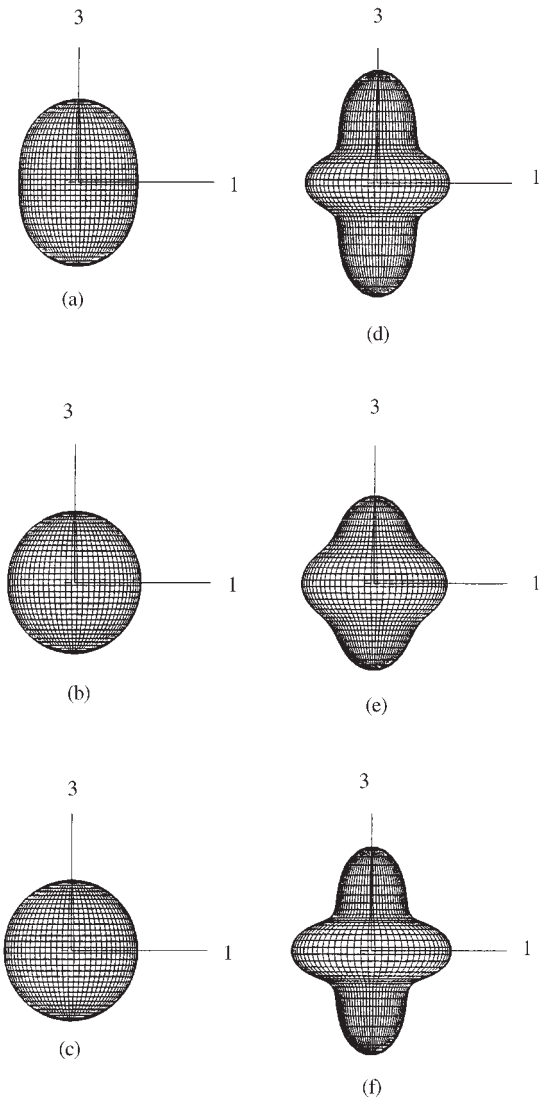

Figure 14. Evolutions of fabric of rank 2 ((a)–(c)) and rank 4 ((d)–(f)) in various loadings for $D_r = 62.3\%$: (a) $\sigma_v = 37.4$–110.72 kPa(L); (b) $\sigma_v = 62.37$ kPa(U); (c) $\sigma_v = 37.4$ kPa(U); (d) $\sigma_v = 37.4$–110.72 kPa(L); (e) $\sigma_v = 62.37$ kPa(U); and (f) $\sigma_v = 37.4$ kPa(U).

6. CONCLUSIONS

This study aimed to investigate the fabric evolution in K_0 loading and unloading. This work made use of a field simulator to control K_0 loading/unloading in large specimens prepared by air-pluviation. Experimentally determined K_0 agreed well with the exiting empirical relations. In each loading stage, wave velocities along various propagation directions were measured. On the

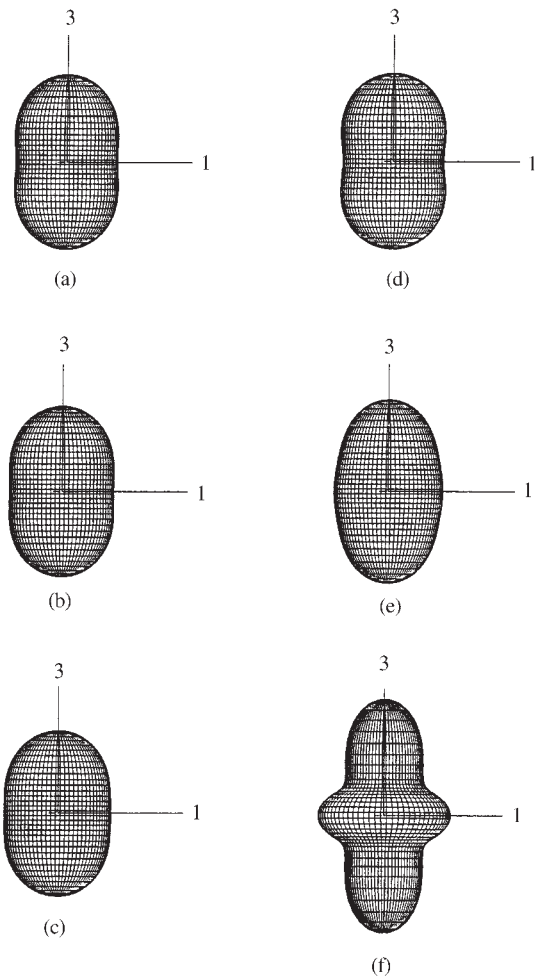

Figure 15. Evolutions of fabric of rank 2 ((a)–(c)) and rank 4 ((d)–(f)) in various loadings for $D_r = 46.5\%$: (a) $\sigma_v = 37.22$–110.54 kPa(L); (b) $\sigma_v = 62.19$ kPa(U); (c) $\sigma_v = 37.22$ kPa(U); (d) $\sigma_v = 37.22$–110.54 kPa(L); (e) $\sigma_v = 62.19$ kPa(U); and (f) $\sigma_v = 37.22$ kPa(U).

basis of the theories of micro-mechanics and wave propagation, the microscopic parameters of the granular assembly were back calculated to investigate the fabric evolution of granular soil during K_0 loading/unloading.

Geometric fabric was modelled by fabric tensors of ranks 2 and 4 separately in this study. The fabric parameter D_{33} (rank 2) or D_{33}/D_{3333} (rank 4) determines the contact normal distribution in a granular assembly. The expression of geometric fabric in fabric of rank 2 with D_{33} only is less complicated but limited; using fabric of rank 4 with D_{33} and D_{3333}, on the other hand, raises the flexibility for describing the shape of contact normal distribution. The relation between the normalized shear stress $(\sigma_v - \sigma_h)/(\sigma_v + \sigma_h)$ and $E(\theta = 45^\circ)$ was examined to explore the influence of shear stress on geometric fabric. The ratio $(\sigma_v - \sigma_h)/(\sigma_v + \sigma_h)$ in the first unloading

Table IV. Stresses and $E(\theta)$ for various cases.

		σ_v (kPa)	(σ_h) (kPa)	τ_{max}/σ_m	Rank	Distribution probability $E(\theta = 0^\circ)$	$E(\theta = 90^\circ)$	$E(\theta = 45^\circ)$
$D_r = 95\%$	Unloading stages	62.78	39.39	0.23	2	0.057	0.091	0.074
					4	0	0.067	0.099
		37.81	28.80	0.14	2	0.046	0.096	0.071
					4	0.001	0.076	0.092
$D_r = 62.3\%$	Unloading stages	62.37	41.71	0.20	2	0.082	0.078	0.080
					4	0.101	0.086	0.072
		37.4	30.26	0.11	2	0.082	0.078	0.080
					4	0.122	0.095	0.063
$D_r = 46.5\%$	Unloading stages	62.19	38.26	0.24	2	0.107	0.066	0.086
					4	0.111	0.068	0.084
		37.22	25.43	0.19	2	0.103	0.083	0.069
					4	0.142	0.083	0.069

Table V. Relation between K_0 and F_H/F_v.

		σ_v (kPa)	K_0	Rank	Statistical parameters F_H	F_v	F_H/F_v
$D_r = 95\%$	Loading stages	37.81–111.13	0.418–0.453	2	0.253	0.245	1.033
				4	0.253	0.258	0.981
	Unloading stages	62.78	0.627	2	0.259	0.232	1.116
				4	0.261	0.242	1.079
		37.81	0.762	2	0.263	0.224	1.174
				4	0.264	0.233	1.133
$D_r = 62.3\%$	Loading stages	37.4–110.72	0.443–0.461	2	0.243	0.264	0.920
				4	0.242	0.257	0.942
	Unloading stages	62.37	0.669	2	0.249	0.252	0.988
				4	0.248	0.249	0.996
		37.4	0.809	2	0.249	0.252	0.988
				4	0.248	0.245	1.012
$D_r = 46.5\%$	Loading stages	37.22–110.54	0.486–0.523	2	0.238	0.274	0.869
				4	0.238	0.275	0.865
	Unloading stages	62.19	0.615	2	0.239	0.271	0.882
				4	0.239	0.270	0.885
		37.22	0.683	2	0.241	0.269	0.896
				4	0.239	0.262	0.912

stage was larger than that in the second unloading stage, while $E(\theta = 45^\circ)$ of rank 4 at the first unloading stage was larger than that at the second unloading. This trend, however, was not predicted by fabric tensor of rank 2 because of its limitation. It reveals the advantage of using the fabric tensor of rank 4 in modelling fabric evolution in spite of its complexity.

By comparing total vertical component F_V and the total horizontal component F_H of geometric fabric, it appears that the ratio F_H/F_V in the unloading stage is significantly larger than in the loading stage. Also, F_H/F_V increases with increasing K_0. The increasing ratio of F_H/F_V during unloading implies increasing relative constraint in lateral directions in order to maintain a K_0 condition. Residual fabric change is accompanied with K_0 unloading. This explains why K_0 in unloading stages was always larger than K_0 in loading stage-fabric evolution is responsible for the change in K_0.

ACKNOWLEDGEMENTS

The National Science Council of the Republic of China under Contract No. NSC90-2211-E-009-068 financially supported this work. This support is gratefully acknowledged.

REFERENCES

1. Cundall PA. Computer simulations of dense sphere assemblies. *Proceedings of the U.S./Japan Seminar on Micromechanics of Granular Materials*, Sendai-Zao, Japan 1987; 113–123.
2. Chang CS, Misra A, Sundaram SS. Properties of granular packings under low amplitude cyclic loading. *Soil Dynamics and Earthquake Engineering* 1991; **10**(4):201–211.
3. Rothenburg L, Bathurst RJ. Micromechanical features of granular assemblies with planar elliptical particles. *Geotechnique* 1992; **42**(1):79–95.
4. Ng TT. Numerical simulations of granular soil using elliptical particles. *Computers and Geotechnics* 1994; **16**(2): 153–169.
5. Emeriault F, Cambou B. Micromechanical modelling of anisotropic non-linear elasticity of granular medium. *International Journal of Solids and Structures* 1996; **33**(18):2591–2607.
6. Lin X, Ng TT. A three-dimensional discrete element model using arrays of ellipsoids. *Geotechnique* 1997; **47**(2): 319–329.
7. Sitharam TG, Nimbkar MS. Micromechanical modelling of granular materials: effect of particle size and gradation. *Geotechnical and Geological Engineering* 2000; **18**(2):91–117.
8. Oda M. Initial fabrics and their relations to mechanical properties of granular material. *Soils and Foundations* 1972; **12**(l):17–36.
9. Lee X, Dass WC. A experimental study of granular packing structure changes under load. *Proceedings of the Second International Conference on Micromechanics of Granular Media*, Birmingham, U.K. 1993; 17–22.
10. Oda M, Konishi J. Microscopic deformation mechanism of granular material in simple shear. *Soils and Foundations* 1974; **14**(4):25–38.
11. Chen YC, Ishibashi I, Jenkins JT. Dynamic shear modulus and fabric: part I, depositional and induced anisotropy. *Geotechnique* 1988; **38**(1):25–32.
12. Ishibashi I, Chen YC, Jenkins JT. Dynamic shear modulus and fabric: part II, stress reversal. *Geotechnique* 1988; **38**(1):33–37.
13. Chien LK, Li JC. Application of electrical conductivity to evaluate the mechanical behaviour of granular material fabric. *Journal of the Chinese Institute of Civil and Hydraulic Engineering* 1990; **2**(1):21–29.
14. Pan YW, Dong JJ. A micromechanics-based methodology for evaluating the fabric of granular material. *Geotechnique* 1999; **49**(6):761–775.
15. Hsu HH, Huang AB. Development of an axisymmetric field simulator for cone penetration tests in sand. *Geotechnical Testing Journal* 1998; **21**(4):348–355.
16. Kanatani K. Distribution of directional data and fabric tensors. *International Journal of Engineering Science* 1984; **22**(2):149–164.
17. Rothenburg L. Micromechanics of idealized granular systems. *Ph.D. Thesis*, Carleton University, Ottawa, 1980.
18. Chang CS, Misra A. Packing structure and mechanical properties of granulates. *Journal of Engineering Mechanics* 1990; **116**(5):1077–1093.
19. Goldberg DE. *Genetic Algorithm in Search. Optimization and Machine Learning*. Addison-Wesley Publishing Company: MA, 1989.

20. Marquardt D. An algorithm for least-squares estimation of nonlinear parameters. *SIAM Journal on Applied Mathematics* 1963; **11**:431–441.
21. Procter DC, Barton RR. Measurements of the angle of interparticle friction. *Geotechnique* 1974; **24**(4):581–604.
22. Oda M. Co-ordination number and its relation to shear strength of granular material. *Soils and Foundations* 1977; **17**(2):29–42.
23. Marsal RJ. Mechanical properties of rockfill. *Embankment Dam Engineering* 1973; 109–145.
24. Yanagisawa E. Influence of void ratio and stress condition on the dynamic shear modulus of granular media. *In Advances in the Mechanics and the Flow of Granular Materials*, Trans Tech Publications, Clausthal-Zellerfeld, Germany, 1983; 947–960.
25. Goddard JD. Nonlinear elasticity and pressure-dependent *wave* speeds in granular media. *Proceedings of the Royal Society of London*, *London*, *Series A* 1990; **430**:105–131.
26. Chang CS, Sundaram SS, Misra A. Initial moduli of particulate mass with frictional contacts. *International Journal for Numerical Analytical Methods in Geomechanics* 1989; **13**(6):629–644.
27. Johnson KL. *Contact Mechanics*. Cambridge University Press: London, 1985.
28. Hardin BO, Richart FE. Elastic wave velocities in granular soils. *Journal of Soil Mechanics Foundation Division*, *Proceedings of ASCE* 1963; **89**(SMI):33–65.
29. Mindlin RD, Deresiewicz H. Elastic spheres in contact under varying oblique forces. *Journal of Applied Mechanics* 1953; **20**(3):327–344.

